

**Title here**

1  
2  
3  
4  
5  
6  
7

Author One,<sup>a</sup> Author Two,<sup>a</sup> Author Three,<sup>b</sup> Author Four,<sup>a</sup> Author Five,<sup>c</sup> Author Six,<sup>d</sup> Author  
Seven,<sup>d</sup> and Author Eight<sup>a,d</sup>

<sup>a</sup> *First Affiliation*

<sup>b</sup> *Second Affiliation*

<sup>c</sup> *Third Affiliation*

<sup>d</sup> *Fourth Affiliation*

<sup>8</sup> Author Five's current affiliation: NCAR, Boulder, Colorado

9 ABSTRACT: Enter the text of your abstract here. This is a sample American Meteorological  
10 Society (AMS) L<sup>A</sup>T<sub>E</sub>X template. This document provides authors with instructions on the use of the  
11 AMS L<sup>A</sup>T<sub>E</sub>X template. Authors should refer to the file amspaper.tex to review the actual L<sup>A</sup>T<sub>E</sub>X code  
12 used to create this document. The template.tex file should be modified by authors for their own  
13 manuscript.

14 Enter significance statement here, no more than 120 words. See [www.ametsoc.org/index.cfm/ams/publications/author-information/significance-statements/](http://www.ametsoc.org/index.cfm/ams/publications/author-information/significance-statements/) for details.

15 Enter BAMS capsule here, no more than 30 words. See [www.ametsoc.org/index.cfm/ams/publications/author-information/formatting-and-manuscript-components/\#capsule](http://www.ametsoc.org/index.cfm/ams/publications/author-information/formatting-and-manuscript-components/\#capsule) for details

## 19 **1. Introduction**

20 It has now become our basic knowledge that the extratropical atmosphere is driven strongly by the  
21 horizontal potential temperature gradient that arises from the differential solar heating (e.g., Lorenz  
22 1955). The horizontal gradient in the potential temperature, often referred to as baroclinicity, is a  
23 measure of upper-level wind steering via thermal wind and a measure of baroclinic instability in  
24 the atmosphere. Baroclinicity in the lower atmosphere in classic theories of atmospheric stability  
25 is measured by a combination of the static stability and horizontal temperature gradient, the latter  
26 of which is equivalent to vertical shear in the horizontal wind through the thermal wind balance  
27 (Charney 1947; Eady 1949). In its original form, the Eady's maximum growth rate for baroclinic  
28 instability  $B_{GRMax}$  is defined by  $B_{GRMax} = 0.31(|f|/N)(\partial U/\partial z)$  in a zonally homogeneous steady  
29 mean state, where  $U$  is the mean zonal flow,  $f$  is the Coriolis parameter, and  $N$  is the Brunt–Väisälä  
30 frequency. Charney's formula is slightly different from the Eady's, but still incorporates the same  
31 effects (Table 1).

32  
33  
34  
35  
36  
37  
38 Lindzen and Farrell (1980) first applied the Eady's parameter to atmospheric data to successfully  
39 estimate the maximum growth rate of baroclinic instability in the troposphere. Hoskins and Valdes  
40 (1990) used its localized version (i.e.,  $U$ ,  $N$ , and  $f$  are all local Eulerian mean values) as the  
41 central parameter in their study of the Northern Hemispheric storm tracks. This local version, or  
42 its simplified version, has been used successfully as an indicator of baroclinic wave generation in  
43 diagnostic studies of stormtracks in recent years as well (Nakamura and Sampe 2002; Nakamura  
44 and Shimpo 2004; Nakamura et al. 2004). In our study, the North Atlantic part of which was  
45 reported in Nakamura and Yamane (2009, hereafter Part I), we define the near-surface baroclinic  
46 vector,  $\mathbf{B} = B^x\mathbf{i} + B^y\mathbf{j}$ , where  $B^x = -(g/\theta N)(\partial\theta/\partial y)$  and  $B^y = (g/\theta N)(\partial\theta/\partial x)$  with  $\theta$  being the  
47 monthly-mean potential temperature at 2 m above the surface, and use it as the central quantity  
48 of the diagnoses. Unless stated otherwise, “anomalies’ ’ refer to deviations from the climatology

Month	EOF1	Split	EOF2	Split	EOF3	EOF4
Jan	29	NG	24	GD	10	5
Feb	39	GD	20	GD	7	6
Mar	31	GD	14	NG	10	6
Apr	23	GD	14	NG	10	7
May	19	GD	12	NG	10	7
Jun	19	GD	12	NG	10	9
Jul	18	NG	13	NG	9	7
Aug	18	NG	13	NG	11	9
Sep	17	NG	13	NG	10	8
Oct	16	NG	13	GD	8	7
Nov	19	NG	16	NG	11	8
Dec	33	GD	18	GD	10	6

TABLE 1. Percentage of variance explained by the first four EOFs for the North Pacific Bx. The degree of separation between EOF1 and EOF2 and EOF2 and EOF3, based on the North et al. (1982) criterion, is indicated by good (GD) and not good or marginal (NG).

hereafter. Though its meridional component does not appear in any classic theory of baroclinic instability, a theory that does incorporate the effect of  $B^y$  shows its important role in enhancing baroclinic wave generation locally to the east of the mean trough (Niehaus 1980). In the North Atlantic storm track region, we indeed found that the substantial zonal gradient in the surface temperature in and around the Labrador Sea plays a major role in the large-scale atmospheric state.

## 2. The sea surface temperature

The sea surface temperature (SST) is an important factor in determining  $\mathbf{B}$  in the storm-track regions (e.g., Hoskins and Valdes 1990; Nakamura et al. 2004; Part I). SST anomalies (SSTAs) around an oceanic front along the Gulf Stream (GS), Kuroshio Extension (KE), or Oyashio Extension (OE) can have a profound impact on  $\mathbf{B}$  along the storm tracks.

### *a. A subtle point*

A subtle but important point that has to be considered carefully in this regard is the spatial scale and the location of SSTAs with respect to the climatology, since it is the anomalous surface temperature gradient whose structure has a spatial scale of the atmospheric Rossby deformation radius that can exert significant influence on the large-scale atmospheric flow.

64 1) CHANGES IN THE TEMPERATURE

65 The high sensitivity of **B** to changes in the temperature contrast across the front and changes  
66 in the width of the front, and the uncertainty in the impact of SSTAs of small spatial scales on  
67 **B** make it difficult to assess the effective **B** anomalies that are attributable to the SSTAs from the  
68 available data. Moreover, it is uncertain exactly how the SSTAs in the presence or absence of the  
69 land surface temperature anomalies may or may not produce **B** anomalies that are significant to the  
70 atmosphere.

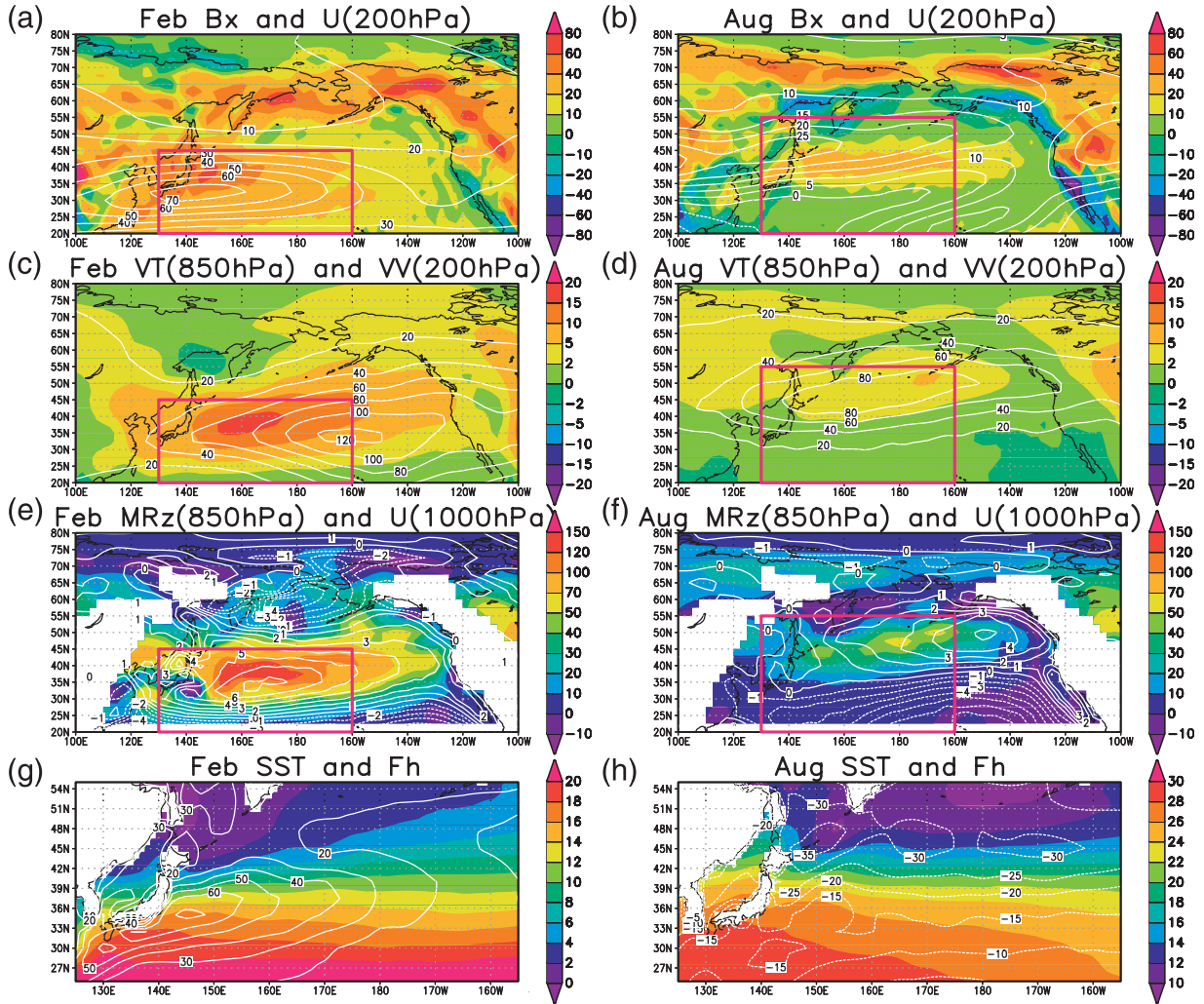
71 *(i) Complicating factor* The complicating factor introduced by the land surface must be taken  
72 into account when studying potential roles of extratropical SSTAs in the extratropical atmospheric  
73 anomalies. Lau (1988) investigated patterns of anomalous storm track activity and associated  
74 low-frequency flow anomalies by computing empirical orthogonal functions (EOFs) for high-  
75 frequency 500-hPa geopotential height for the Northern Hemisphere winters. He found that both  
76 North Atlantic and North Pacific storm tracks have a pattern of meridional shift and a pattern of  
77 increased or decreased eddy activity in the first two EOFs. He also found that these changes in the  
78 storm tracks have symbiotic relationships with the background flows and have substantial impacts  
79 on the mean flow. Part I approached the issue of the stormtrack and low-frequency flow variability  
80 in connection with SSTAs in the extratropics, focusing on **B** as the key parameter of diagnoses,  
81 and found similar patterns of variability in the eddy activity and low-frequency flow in the North  
82 Atlantic basin. Much of this variability was connected to SSTAs in the vicinity of the Gulf Stream  
83 in cold months (Part I). Since the winter North Pacific basin has a storm track and mean flow  
84 that appear to be related to the oceanic fronts, Kuroshio–Oyashio Extensions (KOE) in this case,  
85 in a manner essentially the same as those in the North Atlantic basin related to the GS, we have  
86 attempted to find similar results for the North Pacific basin. In this regard, we have chosen not  
87 to project our results onto the major mode of variability in the extratropical North Pacific basin,  
88 the North Pacific decadal variability (PDV), so that our presentation and discussion are mostly  
89 confined to the wave–mean flow dynamics of monthly time scale or shorter.

90 Our approach to the search for a link between anomalies in the KOE and the overlying atmosphere  
91 is as follows: (i) identify dominant patterns in anomalous **B** in the storm track for each calendar-  
92 month and identify years in which the anomaly fits the pattern well, (ii) composite anomalies in  
93 the monthly-mean circulation and high-frequency transients in the atmosphere to obtain a typical

94 atmospheric state that accompanies the patterns of anomalous  $\mathbf{B}$ , (iii) composite SSTA to obtain  
 95 a typical oceanic state that accompanies and precedes the patterns of anomalous  $\mathbf{B}$ , and (iv) com-  
 96 posite anomalous net surface heat flux that accompanies and precedes the pattern of anomalous  $\mathbf{B}$ .  
 97 With this approach, we obtain typical pictures of anomalous states in the atmosphere and oceans  
 98 with anomalous  $\mathbf{B}$  as their connecting interface. Section 2 describes the data and procedure to  
 99 compute  $\mathbf{B}$ . Section 3 describes the climatology and variance of  $\mathbf{B}$ . Dominant patterns of  $\mathbf{B}$  are  
 100 shown in section 4, followed by composited anomalies in various atmospheric fields and SST in  
 101 section 5. Finally, we present our discussion on the results, examining a potential cause–effect  
 102 relationship between anomalies in the SST and atmosphere in section 6.

111 Figure 1 shows the climatology of  $B_x$ ,  $U^{200}$ ,  $\overline{V'\theta'}^{850}$ ,  $\overline{V'\theta'}^{200}$ ,  $MR^{850}$ ,  $U^{1000}$ , SST, and  $F_h$  for  
 112 February and August as examples of the reference state in the winter and summer. The numeric  
 113 superscript indicates the pressure level in hPa. The seasonal mean is visibly more diffused in  
 114 structure, particularly for  $B_x$ , than those shown in Fig.~1. There are no surprises in the overall  
 115 picture of  $B_x$ . The regions of large land–sea temperature contrast and the oceanic fronts show very  
 116 large  $B_x$  in cold months. The position of  $B_x$  maximum in the storm track region is found along  
 117 the KOE region throughout the year. The zonally elongated band of large  $B_x$  in the storm track is  
 118 generally wider in cold months than in warm months. In fact, large  $B_x$  values that presumably  
 119 accompany the Kuroshio and its extension in the cold months vanish in the summer (Figs. 1a,b).  
 120 The seasonal variation in the  $B_x$  values in the storm track basically follows that of the north–south  
 121 differential heating—largest in the winter and smallest in the summer. As reported by Nakamura  
 122 et al. (2004), the  $U^{200}$  maximum is displaced southward from the  $B_x$  maximum visibly in winter  
 123 months (Fig. 2a), although  $U^{200}$  is generally large over the area of large  $B_x$  in the core of the storm  
 124 track. The southward displacement of the  $U^{200}$  maximum from the  $B_x$  maximum in the storm  
 125 track is less pronounced or even reversed in warmer months (Fig. 2b). We note that the structure  
 126 of the climatological  $B_x$  generally reflects those of  $(\partial\theta^{2m}/\partial y)$  with some exceptions where the  
 127 surface slope contributes significantly to  $B_x$  in isolated areas over the land, most notably around  
 128 the Himalayas.

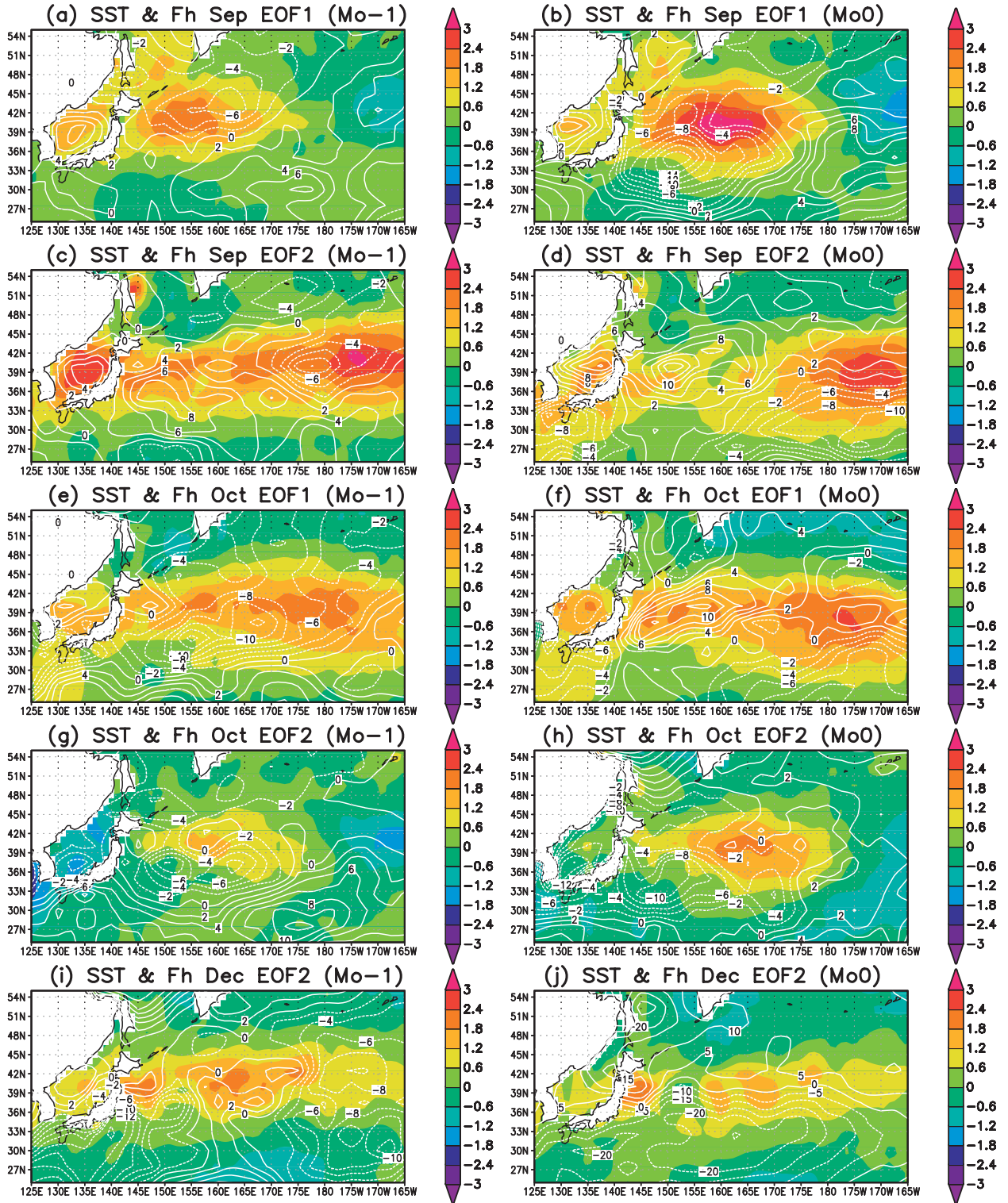
133 The position and structure of the storm track as indicated by  $\overline{V'\theta'}^{850}$  and  $\overline{V'V'}^{200}$  are, at least for  
 134 the winter, essentially the same as those reported in earlier studies on the storm tracks (e.g., Chang  
 135 et al. 2002). The maxima in  $\overline{V'\theta'}^{850}$  and  $\overline{V'V'}^{200}$  are located in the band of large  $B_x$ .



107 FIG. 1. Climatology of  $Bx$  ( $10^{-6} s^{-1}$ , color) and  $U^{200}$  ( $m s^{-1}$ , contours) for (a) February and (b) August;  $\overline{V'\theta'}^{850}$   
 108 ( $K m s^{-1}$ , color) and  $\overline{V'V'}^{200}$  ( $m^2 s^{-1}$ , contours) for (c) February and (d) August;  $MR^{z850}$  ( $10^{-3} m^2 s^{-2}$ , color)  
 109 and  $U^{1000}$  ( $m s^{-1}$ , contours) for (e) February and (f) August; and SST (K, color) and  $F_h$  [ $10^5 J m^{-2} (6 h)^{-1}$ ]  
 110 for (g) February and (h) August. Red rectangles indicate the domain of EOF calculations.

### 136 3. Data and calculation procedures

137 The data used to calculate  $\mathbf{B}$  are the monthly-mean temperature at 2 m above the surface ( $T^{2m}$ )  
 138 and temperature at pressure levels available from the 40-yr European Centre for Medium-Range  
 139 Weather Forecasts (ECMWF) Re-Analysis (ERA-40; Uppala et al.~2005). We chose the ERA-  
 140 40  $T^{2m}$  data rather than the National Centers for Environmental Prediction–National Center for  
 141 Atmospheric Research (NCEP–NCAR) reanalysis products for its explicit inclusion of the observed



131 FIG. 2. As in Fig. 10, but for (a),(b) September EOF1; (c),(d) September EOF2; (e),(f) October EOF1; (g),(h)  
 132 October EOF2; and (i),(j) December EOF2.

142 near-surface temperature in producing the  $T^{2m}$  data. The monthly-mean surface pressure data from  
143 the NCEP–NCAR reanalyses (Kalnay et al. 1996) were used to determine the pressure levels to  
144 be used for  $\mathbf{B}$  calculation, and to calculate  $\theta$  at 2 m above the surface from  $T^{2m}$ . We used the  
145 NCEP–NCAR surface pressure data for convenience, since we had already compiled the dataset for  
146 calculating transient eddy fluxes to be mentioned later and the ERA-40 surface pressure data are  
147 not readily available. We later compared the NCEP–NCAR monthly-mean sea level pressure with  
148 that of ERA-40, and found the difference between the two products to be immaterial for the purpose  
149 of the current study. We also used ERA-40 monthly-mean horizontal wind and geopotential height  
150 at pressure levels, net surface heat flux, Fh (the sum of latent heat flux, sensible heat flux, solar  
151 radiation, and the thermal radiation), and Hadley Centre sea surface temperature data (Rayner et  
152 al. 2003) to compile anomaly composites accompanying anomalous patterns in  $\mathbf{B}$ . In addition, we  
153 used 6-hourly temperature and wind data from the NCEP–NCAR reanalyses to compute various  
154 eddy fields. The accuracy of the Fh data used here is, as true for other reanalyses surface heat flux  
155 products, may not be so high to produce reliable anomaly composites.

156 We computed  $\mathbf{B}$  near the surface by calculating the horizontal gradient in  $\theta^{2m}$ , using the centered  
157 finite differencing, and calculating  $N$  from the lowest three vertical pressure levels that are location  
158 dependent because of topography. Both  $\nabla\theta^{2m}$  and  $N$  were calculated locally as in Hoskins and  
159 Valdes (1990) and Nakamura and Shimpo (2004). The entire 45 yr from September 1957 to August  
160 2002 were used for the Northern Hemisphere. To resolve the dominant modes in  $\mathbf{B}$  arising from  
161 the land–sea temperature contrast, one may need much higher horizontal resolution in the data.  
162 The relatively coarse horizontal resolution of the data may artificially suppress the significance of  
163 the variability associated with the land–sea temperature contrast. One should keep this limitation in  
164 mind. The 6-hourly bandpassed (period of 2–7 days) eddy fields and ultra-low-frequency (period  
165 of 30 days and longer) background fields were computed from the NCEP–NCAR reanalyses, using  
166 simple time filters (Lau and Lau 1984) first. The filtered time series were then visually examined  
167 against the raw time series and, then, used to calculate the slowly evolving bandpassed meridional  
168 velocity variance ( $\overline{V'V'}$ ), meridional temperature flux ( $\overline{V'\theta'}$ ), and the three-dimensional transient  
169 wave activity flux defined on a zonally varying basic state by Plumb (1986). The wave activity  
170 flux consists of the zonal and meridional advective fluxes (MU and MV), the zonal and meridional  
171 radiative fluxes (MRx and MRy), and the radiative vertical flux (MRz). The flux is essentially

172 the Eliassen–Palm flux (Eliassen and Palm 1961) in a zonally inhomogeneous mean flow (Plumb  
 173 1986). The wave activity flux was calculated from February 1948 to November 2004 only for the  
 174 extratropics poleward of 20° latitude. Also, it was calculated only from 850 to 30 hPa because  
 175 of the double differentiation with respect to pressure required for the calculation. The flux of  
 176 particular interest in this study is the vertical component. Here  $MR^z$  is defined by

$$MR^z = \frac{p f \cos \phi}{p^0 |\nabla h \bar{q}| (d\theta_0/dz)} \left( \frac{\partial \bar{q}}{\partial x} \overline{U'\theta'} + \frac{\partial \bar{q}}{\partial y} \overline{V'\theta'} \right),$$

177 where  $q$  is quasigeostrophic potential vorticity,  $p$  is the pressure,  $p^0$  is the reference surface  
 178 pressure set to 1000 hPa here,  $\theta_0$  is the area-weighted ultra-low-frequency hemispheric mean  
 179 potential temperature at each height,  $u_9$  is the bandpassed potential temperature, and  $z$  is the  
 180 geopotential height. An overbar denotes an ultra-low frequency component and a prime denotes  
 181 bandpassed component. The 6-hourly time series of wave fluxes was computed by using the time  
 182 series of ultra-low-frequency fields as the basic-state and high-frequency fields as eddies. In short,  
 183 the time series was calculated by changing the meaning of an overbar from the time mean state to  
 184 an ultra-low-frequency state, and changing the meaning of a prime from a departure from the mean  
 185 to a high-frequency state. The 6-hourly eddy time series was averaged over each month to produce  
 186 monthly-mean time series. This dataset allows us to examine anomalous eddy fields accompanying  
 187 anomalous  $\mathbf{B}$  in specific months. The climatology for the eddy fields was computed from 46 yr,  
 188 January 1958 to December 2003. The calculation of the wave activity and its flux is described in  
 189 detail by Nakamura et al. (2010).

#### 190 4. Climatology and variance

191 The climatology and variance of  $B_x$  and  $B_y$  were computed for each calendar month and  
 192 examined closely for their spatial and temporal structures. The monthly climatology, rather than  
 193 the seasonal climatology, is used as the reference in our study, to avoid contamination of the  
 194 diagnostic results arising from differences in the climatology between two successive months.  
 195 Unlike in the North Atlantic basin reported in Part I, we found the impact of  $B_y$  variations on the  
 196 large-scale atmospheric state in the North Pacific basin much weaker than that of  $B_x$  variations,  
 197 presumably because of the more zonal orientation of the KOE in comparison to the Gulf Stream

198 and North Atlantic Current. In the following, thus, we focus our presentation on the climatology  
199 and variations of  $Bx$  and their impact on the large-scale atmospheric state.

200 Sample citations: Becker and Schmitz (2003), Knutti et al. (2008), and (Meixner et al. 2002;  
201 Kuji and Nakajima 2002; Emery et al. 1986).

202 We thank two anonymous reviewers for their comments, which helped to improve the manuscript.  
203 Start data availability statement here.

## 204 **5. Appendix Title**

### 205 *Appendix section head*

206 Here is a sample appendix with an equation [see Eq. (1)]. Lorem ipsum dolor sit amet,  
207 consectetur adipiscing elit, sed do eiusmod tempor incididunt ut labore et dolore magna aliqua. Ut  
208 enim ad minim veniam, quis nostrud exercitation ullamco laboris nisi ut aliquip ex ea commodo  
209 consequat.

$$\frac{p f \cos \phi}{p^0 |\nabla h \bar{q}| (d\theta_0/dz)} \quad (1)$$

210 Lorem ipsum dolor sit amet, consectetur adipiscing elit, sed do eiusmod tempor incididunt ut  
211 labore et dolore magna aliqua. Ut enim ad minim veniam, quis nostrud exercitation ullamco laboris  
212 nisi ut aliquip ex ea commodo consequat. Duis aute irure dolor in reprehenderit in voluptate velit  
213 esse cillum dolore eu fugiat nulla pariatur. Excepteur sint occaecat cupidatat non proident, sunt in  
214 culpa qui officia deserunt mollit anim id est laborum.

215 Lorem ipsum dolor sit amet, consectetur adipiscing elit, sed do eiusmod tempor incididunt ut  
216 labore et dolore magna aliqua. Ut enim ad minim veniam, quis nostrud exercitation ullamco laboris  
217 nisi ut aliquip ex ea commodo consequat. Here is an example appendix figure (see Fig. 3).

## 218 **6. Second Appendix Title**

### 219 *a. Sample appendix section head*

220 Lorem ipsum dolor sit amet, consectetur adipiscing elit, sed do eiusmod tempor incididunt ut  
221 labore et dolore magna aliqua. Ut enim ad minim veniam, quis nostrud exercitation ullamco laboris  
222 nisi ut aliquip ex ea commodo consequat [see Eq. (2)]. Duis aute irure dolor in reprehenderit in  
223 voluptate velit esse cillum dolore eu fugiat nulla pariatur. Excepteur sint occaecat cupidatat non  
224 proident, sunt in culpa qui officia deserunt mollit anim id est laborum.

$$\left( \frac{\partial \bar{q}}{\partial x} U' \theta' + \frac{\partial \bar{q}}{\partial y} V' \theta' \right) \quad (2)$$

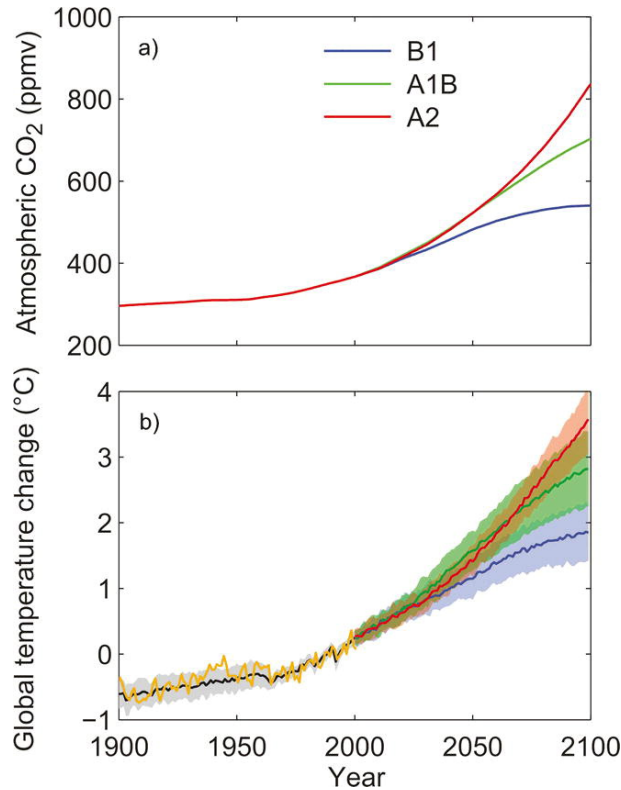


FIG. 3. Here is an appendix, single column figure caption.

225 Lorem ipsum dolor sit amet, consectetur adipiscing elit, sed do eiusmod tempor incididunt ut  
 226 labore et dolore magna aliqua. Ut enim ad minim veniam, quis nostrud exercitation ullamco laboris  
 227 nisi ut aliquip ex ea commodo consequat. Duis aute irure dolor in reprehenderit in voluptate velit  
 228 esse cillum dolore eu fugiat nulla pariatur. Excepteur sint occaecat cupidatat non proident, sunt  
 229 in culpa qui officia deserunt mollit anim id est laborum. Lorem ipsum dolor sit amet, consectetur  
 230 adipiscing elit, sed do eiusmod tempor incididunt ut labore et dolore magna aliqua. Ut enim ad  
 231 minim veniam, quis nostrud exercitation ullamco laboris nisi ut aliquip ex ea commodo consequat.  
 232 Duis aute irure dolor in reprehenderit in voluptate velit esse cillum dolore eu fugiat nulla pariatur.  
 233 Excepteur sint occaecat cupidatat non proident, sunt in culpa qui officia deserunt mollit anim id est  
 234 laborum.

235 *b. Sample appendix section head*

236 Second appendix example. Here an example appendix table (see Table 2).

Month	Yr of positive phase
Jan	1961, 1969, 1978, 1979, 1988, 1990, 1992, 1994
Feb	1964, 1977, 1978, 1980, 1983, 1986, 1988, 2000, 2001
Mar	1970, 1973, 1979, 1980, 1984, 1988, 2000
Apr	1959, 1961, 1962, 1963, 1968, 1972, 1983, 2002
May	1971, 1984, 1993, 1996, 2000
Jun	1981, 1983, 1984, 1993, 1998
Jul	1961, 1972, 1973, 1978, 1994, 2000
Aug	1967, 1970, 1973, 1978, 1994, 1999
Sep	1975, 1977, 1988, 1989, 1994, 1998, 1999
Oct	1962, 1977, 1998, 1999, 2001
Nov	1985, 1986, 1987, 1988, 1991, 1998
Dec	1957, 1968, 1972, 1978, 1979, 1990

TABLE 2. Years selected for anomaly composites for the positive phase of  $B^x$  EOF1.

## 237 References

- 238 Becker, E., and G. Schmitz, 2003: Climatological effects of orography and land–sea heating  
239 contrasts on the gravity wave–driven circulation of the mesosphere. *J. Atmos. Sci.*, **60**, 103–118,  
240 [https://doi.org/10.1175/1520-0469\(2003\)060<0103:CEOAL>2.0.CO;2](https://doi.org/10.1175/1520-0469(2003)060<0103:CEOAL>2.0.CO;2).
- 241 Emery, W. J., A. C. Thomas, M. J. Collins, W. R. Crawford, and D. L. Mackas, 1986: An objective  
242 method for computing advective surface velocities from sequential infrared satellite images. *J.*  
243 *Geophys. Res.*, **91**, 12 865–12 878, <https://doi.org/10.1029/JC091iC11p12865>.
- 244 Knutti, R., and Coauthors, 2008: A review of uncertainties in global temperature projections over  
245 the twenty-first century. *J. Climate*, **21**, 2651–2663, <https://doi.org/10.1175/2007JCLI2119.1>.
- 246 Kuji, M., and T. Nakajima, 2002: Retrieval of cloud geometrical parameters using remote sensing  
247 data. *11th Conf. on Cloud Physics*, Ogden, UT, Amer. Meteor. Soc., JP1.7, <http://ams.confex.com/ams/pdfpapers/39550.pdf>.
- 248
- 249 Meixner, T., L. A. Bastidas, H. V. Gupta, and R. C. Bales, 2002: Multicriteria parameter estimation  
250 for models of stream chemical composition. *Water Resour. Res.*, **38**, 1027, <https://doi.org/10.1029/2000WR000112>.
- 251